

000 001 002 003 004 005 006 007 008 009 010 011 012 013 014 015 016 017 018 019 020 021 022 023 024 025 026 027 028 029 030 031 032 033 034 035 036 037 038 039 040 041 042 043 044 045 046 047 048 049 050 051 052 053 ADAPTIVE FOURIER MAMBA OPERATORS

Anonymous authors

Paper under double-blind review

ABSTRACT

Accurately solving partial differential equations (PDEs) on arbitrary geometries and a variety of meshes is an important task in science and engineering applications. In this paper, we propose Adaptive Fourier Mamba Operators (AFMO), which integrates reproducing kernels for state-space models (SSMs) rather than the kernel integral formulation of SSMs. This is achieved by constructing Takenaka-Malmquist systems for the PDEs. AFMO offers new representations that align well with the adaptive Fourier decomposition (AFD) theory and can approximate the solution manifold of PDEs on a wide range of geometries and meshes. In several challenging benchmark PDE problems in the fields of fluid physics, solid physics, and finance on point clouds, structured meshes, regular grids, and irregular domains, AFMO consistently outperforms state-of-the-art solvers in terms of relative L^2 error. Overall, this work presents a new paradigm for designing explainable neural operator frameworks.

1 INTRODUCTION

A wide range of scientific and engineering phenomena, including fluid dynamics, heat and mass transport, structural mechanics, and cell growth, can be characterized and modeled by partial differential equations (PDEs). Most nonlinear PDEs do not have analytical solutions and need to be solved numerically. Traditional discretization-based approaches for solving PDEs can be computationally expensive. To speed up the solution process, neural operators have recently been proposed as an extension of neural networks to learn the infinite-dimensional solution operators of various PDE problems. It has been proven that, with finite-dimensional solutions as training data, neural operators can accurately learn the infinite-dimensional solution space. Once learned, neural operators are mesh-independent, so neural operators trained on coarse grids can generalize to finer grids.

Frequency-based neural operators, such as Fourier neural operator (FNO) (Li et al., 2020), wavelet neural operator (WNO) (Tripura & Chakraborty, 2023), multiwavelet transform (MWT) (Gupta et al., 2021), U-shaped neural operator (Rahman et al., 2022), spectral neural operator (Fanaskov & Oseledets, 2023), and latent spectral model (LSM) (Wu et al., 2023), are attractive since the solution space of many PDEs can be naturally expressed in spectral bases. Frequency-based neural operators approximate the PDE solutions by learning how frequencies evolve, and nonlinear terms become convolution in the associated frequency domain. However, the performance of existing frequency-based neural operators may deteriorate in irregular geometries (Li et al., 2023), as their associated bases could lose orthogonality and eigenfunction properties in irregular domains (Lingsch et al., 2023; Chen et al., 2024). As a result, retaining these important properties for kernels and bases for irregular domains is critical.

Along this line, a recently proposed neural operator solver, latent Mamba operator (LaMO) (Tiwari et al., 2025), shows great promise in capturing PDE solutions in irregular domains. LaMO integrates the efficiency of state-space models (SSMs) in latent space with the expressive power of kernel integral formulations in neural operators. Although the selective convolution kernels utilized in LaMO can effectively capture PDE solutions on the irregular domain, their lack of orthogonality property may lead to spectral mixing. Furthermore, since the kernels in LaMO are finite-order linear dynamic filters (Gu & Dao, 2023), its finite-order state-space dynamics may induce a low-pass filtering bias, leading to poor recovery of high-frequency and singular features (Gu et al., 2021; Gu & Dao, 2023). In the illustrative experiments discussed in Appendix B, we show that LaMO suffers from deviation in the propagation of high-frequency perturbations for 1-D advection PDE, and it

054 fails to capture the singularities in 2-D Darcy flow equation with fractal noise as the permeability
 055 field.

056 Recognizing the fact that LaMO lacks frequency-domain implementation, here we propose Adaptive
 057 Fourier Mamba Operator (AFMO), a novel neural operator architecture that synergizes an adaptive
 058 Fourier decomposition with the efficiency of structured SSMs in the frequency domain (Gu & Dao,
 059 2023; Parnichkun et al., 2024). AFMO parameterizes the SSM transfer function in a Takenaka-
 060 Malmquist (TM) system in a reproducing kernel Hilbert space (RKHS), thus allowing state-free
 061 kernel construction and inference directly on the spectrum. The Mamba blocks in AFMO serve as
 062 rational filters while retaining linear-time selective scanning. Furthermore, it turns out that AFMO
 063 structure resembles adaptive Fourier decomposition (AFD), a novel signal decomposition technique
 064 achieving higher accuracy and significant computational speedup compared to conventional signal
 065 decomposition methods (Qian, 2010; Qian et al., 2012). The architecture and design of AFMO is
 066 fully guided by the AFD theory, thereby improving the mathematical explainability and groundness
 067 of AFMO,

068 Overall, our key contributions are summarized as follows:
 069

- 070 AFMO is the first neural operator which explicitly incorporates TM systems and Fourier-
 071 based methods into the Mamba structure. AFMO accurately solves the PDE problems on
 072 diverse geometries and effectively handles singularities and long-range dependencies of
 073 PDE solutions, Furthermore, we develop theoretical foundations for AFMO and prove that
 074 AFMO performs AFD approximation of PDE solutions.
- 075 The design of every component of AFMO is fully guided by the AFD theory, leading
 076 to a mathematically interpretable and grounded architecture. Using a TM layer, AFMO
 077 projects the input into TM systems in a Hardy space, and constructs the reproducing kernels
 078 from adaptively selected poles. These adaptive poles serve to construct the reproducing
 079 kernels adaptively. We demonstrate the importance of utilizing adaptive poles as opposed
 080 to fixed poles and investigate how the number of adaptive poles influences the performance
 081 of AFMO.
- 082 AFMO outperforms state-of-the-art neural operator solvers in terms of accuracy across a
 083 diverse set of benchmark PDE problems, including plasticity, elasticity, airfoil, pipe flow,
 084 Navier-Stokes, and Darcy flow on various geometries. It also achieves outstanding perfor-
 085 mance in financial applications, such as solving the Black-Scholes equation for the Euro-
 086 pean option pricing problem.

087 2 RELATED WORK

088 **Frequency-based neural operators.** Early advancements in operator learning exploited spectral
 089 decompositions to encode global information efficiently. A notable example is FNO (Li et al.,
 090 2020), which parameterizes integral kernels in the Fourier domain to enable resolution-invariance.
 091 However, FNO does not generalize well to irregular geometries (Li et al., 2020). Later, Geo-FNO
 092 (Li et al., 2023) was proposed to solve PDEs on general geometries. U-FNO (Wen et al., 2022)
 093 introduced architectural modifications to better capture localized details while maintaining FNO’s
 094 global properties. Meanwhile, F-FNO (Tran et al., 2021) generalizes the FNO architecture for more
 095 efficient spectral layers and deeper architectures. On the other hand, neural operators based on the
 096 wavelet transform include WNO (Tripura & Chakraborty, 2023), MWT (Gupta et al., 2021), Padé
 097 (Gupta et al., 2022), and CMWNO (Xiao et al., 2023a). Fourier and wavelet transforms are both
 098 special cases of spectral decomposition, and neural operators based on spectral decomposition has
 099 recently been proposed (Fanaskov & Oseledets, 2023).

100 **Attention-based neural operators.** Attention mechanisms have been widely studied in neural op-
 101 erator domain. Some of the notable works include orthogonal attention (Xiao et al., 2023b), physics-
 102 cross-attention (Wang & Wang, 2024), and nonlocal attention (Yu et al., 2024). The Transformer
 103 structure is also a promising building block for neural operators. Some of the related works in-
 104 clude OFormer (Li et al., 2022), LSM (Wu et al., 2023), and Transolver (Wu et al., 2024). However,
 105 Transformers struggle to capture kernel integral transforms efficiently in complex, high-dimensional
 106 continuous PDEs (Guibas et al., 2021).

108 **SSM-based neural operators.** To address the computational inefficiency of Transformer-based
 109 neural operators, SSM and Mamba emerge as promising architectures for neural operator designs
 110 (Tiwari et al., 2025). Previous studies of SSM-based neural operators (Zheng et al., 2024; Cheng
 111 et al., 2024; Hu et al., 2024; Tiwari et al., 2025) have been applied to nonlinear PDEs on irregular
 112 geometries and dynamical systems. These works incorporate traditional SSMs with different scan
 113 strategies without considering the information in the frequency domain. On the other hand, our
 114 AFMO considers the frequency information via its explicit kernel and SSMs from a transfer function
 115 perspective (Parnichkun et al., 2024).

116

117 3 ADAPTIVE FOURIER MAMBA OPERATOR

119 3.1 PROBLEM STATEMENT

121 We frame our task as learning a solution operator for a family of parametric PDEs. In general,
 122 consider a PDE defined on a spatial domain $\Omega \subset \mathbb{R}^d$ and a time interval $(0, T]$:

$$124 \quad \mathcal{L}_a[u(x, t)] = f(x, t), \quad \forall (x, t) \in D \times (0, T], \quad (1)$$

125 which is subject to a set of initial and boundary conditions. Here, the parameter function $a \in \mathcal{A}$
 126 specifies the coefficients and initial and boundary conditions of Equation 1. In operator learning,
 127 our goal is to construct an accurate approximation for $\mathcal{G} : \mathcal{A} \rightarrow \mathcal{F}(D \times [0, T])$, which maps the
 128 parameter function a to the corresponding solution function $u(x, t) \in \mathcal{F}$, via a parametric mapping
 129 \mathcal{G}_θ . The aim is to learn θ such that $\mathcal{G}_\theta \approx \mathcal{G}$ from a set of training data $\{(a_j, u_j)\}_j$.

131 3.2 AFMO ARCHITECTURE

133 AFMO is a novel neural operator architecture that synergizes the mathematical groundness of AFD
 134 theory with the efficiency of structured SSMs in the frequency domain (Gu & Dao, 2023; Par-
 135 nichkun et al., 2024). Different from LaMO (Tiwari et al., 2025), which compresses the physical
 136 tokens into a fixed-size latent representation, AFMO utilizes a multi-layer fully-connected feed-
 137 forward neural network (MLP) to first map the encoded tokens to their counterparts on the reproducing
 138 kernel Hilbert space (RKHS), and then iteratively refine them by a series of processing blocks. Each
 139 block uniquely integrates two components: (i) a TM layer containing global spectral transform via
 140 data-dependent TM bases, and (ii) a bidirectional SSM (Gu et al., 2021; Gu & Dao, 2023) parame-
 141 terized by transfer functions in the frequency domain (Parnichkun et al., 2024) to efficiently capture
 142 long-range dependencies within the RKHS.

143

144 Neural architecture. Given the parameter function (input) a , the output of AFMO, denoted as
 145 $\hat{u}_{N, \theta}$, is:

$$146 \quad \hat{u}_{N, \theta} = \mathcal{G}_\theta(a) = (\mathcal{Q} \circ \mathcal{S}^N \circ \mathcal{L}^N \circ \dots \circ \mathcal{S}^1 \circ \mathcal{L}^1 \circ \mathcal{R} \circ \mathcal{P})(a), \quad (2)$$

147 where \circ is the function composition, N is the number of processing blocks, \mathcal{P} is the lifting operator
 148 which encodes into a lower-dimensional space (maps the input to the first latent representation \mathbf{z}_0)
 149 (Tiwari et al., 2025; Li et al., 2020), \mathcal{Q} is the corresponding projection operator mapping the lower-
 150 dimensional space back to the original space (maps the final latent representation \mathbf{z}_{N+1} to the output)
 151 (Tiwari et al., 2025; Li et al., 2020), \mathcal{R} is a multi-layer neural network mapping the physical token
 152 to an RKHS, $\mathcal{L}^i = \text{SSM}^i \circ \text{TM}^i$ ($i = 1, \dots, N$) is the processing block of AFMO (which consists
 153 of a TM layer and a bidirectional SSM), and \mathcal{S}^i ($i = 1, \dots, N$) are aggregation layers with skip
 154 connections. These aggregation layers not only receive the final output from the layer sequence but
 155 also have access to the intermediate outputs from each of the preceding layers.

156

157 The lifting operator, \mathcal{P} , projects the N_s physical token inputs into a compressed set of M encoded
 158 tokens, where $M \ll N_s$. This projection is achieved via a cross-attention mechanism. A learnable
 159 query array, $\mathbf{L} \in \mathbb{R}^{M \times D_{\text{embed}}}$, acts as the query. The key and value pairs are constructed by combining
 160 a linear projection of the input features \mathbf{x}_{phys} with a positional embedding of their coordinates \mathbf{g}_{phys}
 161 generated by a positional encoding network PEN. Here, $\mathbf{x}_{\text{phys}} \in \mathbb{R}^{N_s \times D_{\text{in}}}$ stacks the feature vectors
 $\{\mathbf{x}_i\}_{i=1}^{N_s}$ and $\mathbf{g}_{\text{phys}} \in \mathbb{R}^{N_s \times d}$ stacks the coordinates $\{\mathbf{g}_i\}_{i=1}^{N_s}$, and the physical token is essentially

162 pair $(\mathbf{g}_i, \mathbf{x}_i)$. The process for generating the initial representation \mathbf{z}_0 is formally defined as:
 163

$$\begin{aligned} 164 \mathbf{kv} &= \text{Linear}(\mathbf{x}_{\text{phys}}) + \text{PEN}(\mathbf{g}_{\text{phys}}), \\ 165 \mathbf{z}'_0 &= \text{CrossAttn}(\text{query} = \mathbf{L}, \text{key} = \mathbf{kv}, \text{value} = \mathbf{kv}), \\ 166 \mathbf{z}_0 &= \mathbf{z}'_0 + \text{FFN}(\mathbf{z}'_0), \end{aligned} \quad (3)$$

168 where the output of the cross-attention module is processed through a residual connection and a
 169 standard feed-forward network FFN.
 170

171 **The mapping operator**, denoted by \mathcal{R} , acts on the encoded representation produced by the lifting
 172 operator \mathcal{P} , which transforms this discrete encoded tokens into a representation within a continuous
 173 function space. Let $\mathbf{z}_0 \in \mathbb{R}^{M \times D_{\text{embed}}}$ be the set of encoded tokens generated by \mathcal{P} , the operator
 174 $\mathcal{R} : \mathbb{R}^{M \times D_{\text{embed}}} \rightarrow \mathcal{H}$ maps this representation to its counterpart in an RKHS \mathcal{H} . This mapping is
 175 typically implemented as a multi-layer fully-connected feedforward network MLP, which processes
 176 each token independently as:
 177

$$\mathbf{z}_1 = \mathcal{R}(\mathbf{z}_0) = \text{MLP}(\mathbf{z}_0), \quad (4)$$

178 where \mathbf{z}_1 denotes the projected tokens in the RKHS. We remark that, the mapping operator \mathcal{R} maps
 179 the encoded tokens \mathbf{z}_0 to the new tokens \mathbf{z}_1 in \mathcal{H} without knowing the physical information \mathbf{x}_{phys}
 180 and \mathbf{g}_{phys} .
 181

182 **The TM layer**, denoted by TM^i ($i = 1, \dots, N$), performs a global convolution via a spectral
 183 transform, where the reproducing kernels and TM bases are constructed from data-dependent poles.
 184 To define the reproducing kernels, we parameterize a small MLP to predict a set of i complex values
 185 called ‘‘poles’’ $\{a_k\}_{k=1}^i$ (denoted as $a_{1:i}$) located in the unit disk $\mathbb{D} = \{z \in \mathbb{C} : |z| < 1\}$ from tokens
 186 \mathbf{z}_i . Once we have the set of poles, we can explicitly define the reproducing kernel $K_a(z)$ as:
 187

$$K_a(z) = \frac{1}{1 - \bar{a}z}, \quad (5)$$

189 where $z \in \mathcal{H}$ and a is a single pole satisfying $|a| < 1$. Intuitively, we remark that each pole can be
 190 viewed as a ‘‘tuning knob’’ that selects a particular spatial pattern in the solution, with its location in
 191 the complex plane controlling how localized that pattern is. Adaptive poles allow AFMO to survey
 192 more heavily in regions where the parameters change rapidly, while using fewer poles in smooth
 193 regions. Across layers, the poles evolve from broad, coarse patterns in early layers to more refined,
 194 problem-specific patterns in deeper layers.
 195

196 To generalize on irregular geometries, the kernels in Equation 5 need to be modified to become
 197 orthonormal. These modified kernels are also known as the TM bases due to their deep connection
 198 to TM systems. The first basis, denoted as \mathcal{B}_1 , is simply the normalized kernel of Equation 5
 199 with pole a_1 as $\mathcal{B}_1(z; a_1) = \frac{\sqrt{1-|a_1|^2}}{1-\bar{a}_1z}$. Then, we start with $\frac{\sqrt{1-|a_2|^2}}{1-\bar{a}_2z}$, but it is not orthogonal to
 200 \mathcal{B}_1 . We reach the orthogonality by subtracting its projection onto \mathcal{B}_1 , and we get $\mathcal{B}_2(z; a_{1:2}) =$
 201 $\frac{\sqrt{1-|a_2|^2}}{1-\bar{a}_2z} \left(\frac{z-a_1}{1-\bar{a}_1z} \right)$ after normalization. This way, the bases \mathcal{B}_i are finally formulated as:
 202

$$\mathcal{B}_i(z; a_{1:i}) = \frac{\sqrt{1-|a_i|^2}}{1-\bar{a}_i z} \prod_{j=1}^{i-1} \frac{z-a_j}{1-\bar{a}_j z}, \quad (6)$$

203 where $z \in \mathcal{H}$ and $a_{1:i}$ are poles learned by the small MLP satisfying $|a_k| < 1$ for $k = 1, \dots, i$.
 204 Overall, the i -th TM layer TM^i applies a small MLP $\mathbf{z}_i \mapsto a_{1:i}$, and then construct the TM bases
 205 \mathcal{B}_i according to 6. We remark that, the tokens \mathbf{z}_i will be kept as the input of SSM^i along with the
 206 TM bases \mathcal{B}_i .
 207

208 **Bidirectional SSM block** is effective in solving PDEs on irregular geometries (Tiwari et al., 2025)
 209 and employs inherent kernel integrals. However, this inherent kernel does not contain information
 210 in the frequency domain, thereby falling short in capturing high-frequency and singular features. To
 211 address this limitation, we utilize the transfer function in training SSMs in the frequency domain
 212 (Parnichkun et al., 2024). The SSM block SSM^i generates the spectrum of output in the frequency
 213 domain $Y_i(e^{i\omega})$ as the product of the spectrum of input $Z(e^{i\omega})$ and the transfer function $H_i(e^{i\omega})$,
 214

i.e., $Z(e^{i\omega})H_i(e^{i\omega})$. We point out that the output is essentially the coefficient of discrete AFD operation with the form $\langle \mathbf{z}_i, \mathcal{B}_i \rangle$ (Qian, 2010; Qian et al., 2011), where the inner product is defined as $\langle x, f \rangle = \frac{1}{N} \sum_{n=0}^{\tilde{N}-1} x[n] \overline{f(e^{i2\pi n/\tilde{N}})}$. Here, \tilde{N} denotes the length of signal $x = \{x[n]\}_{n=0}^{\tilde{N}-1}$.

Let us consider the impulse response h_i of SSM block SSM^i (linear time-invariant system) as:

$$h_i[n] = \frac{1}{2\pi} \int_0^{2\pi} \overline{\mathcal{B}_i(e^{i\omega}; a_{1:i})} e^{i\omega n} d\omega. \quad (7)$$

Then, the corresponding transfer function H_i can be obtained as:

$$H_i(e^{i\omega}) = \overline{\mathcal{B}_i(e^{i\omega}; a_{1:i})}. \quad (8)$$

By setting the transfer function of SSM to be Equation 8, the SSM block computes a correlation of the input \mathbf{z}_i and \mathcal{B}_i :

$$Y_i(e^{i\omega}) = H_i(e^{i\omega})X(e^{i\omega}) = \overline{\mathcal{B}_i(e^{i\omega}; a_{1:i})} X(e^{i\omega}) \quad (9)$$

in the frequency domain. In the time domain, Equation 9 leads to the update of \mathbf{z}_i :

$$\hat{\mathbf{z}}_{i+1}[\ell] = (h_i * \mathbf{z}_i)[\ell] = \sum_{n=0}^{M-1} \mathbf{z}_i[n] \overline{\mathcal{B}_i(e^{i2\pi(n-\ell)/M}; a_{1:i})}, \quad (10)$$

where ℓ denotes the time shift in the correlation operations. The zero-lag sample gives the final output:

$$\hat{\mathbf{z}}_{i+1}[0] = (h_i * \mathbf{z}_i)[0] = \sum_{n=0}^{M-1} \mathbf{z}_i[n] \overline{\mathcal{B}_i(e^{i2\pi n/M}; a_{1:i})} = \langle \mathbf{z}_i, \mathcal{B}_i \rangle. \quad (11)$$

Aggregation layers \mathcal{S}^i has N neural layers and combines the skip connection \mathbf{z}_i with the intermediate outputs $\hat{\mathbf{z}}_{i+1}[0] = \mathcal{L}^i(\mathbf{z}_i)$ and $\mathcal{B}_i = \text{TM}^i(\mathbf{z}_i)$:

$$\begin{aligned} \mathbf{z}_2 &= \mathcal{S}^i(\mathbf{z}_1, \hat{\mathbf{z}}_2[0], \mathcal{B}_1) = \hat{\mathbf{z}}_2[0] \odot \mathcal{B}_1 \quad \text{for } i = 1, \\ \mathbf{z}_{i+1} &= \mathcal{S}^i(\mathbf{z}_i, \hat{\mathbf{z}}_{i+1}[0], \mathcal{B}_i) = \mathbf{z}_i + (\hat{\mathbf{z}}_{i+1}[0] \odot \mathcal{B}_i) \quad \text{for } i > 1, \end{aligned} \quad (12)$$

where \odot denotes the element-wise (Hadamard) product.

Output. Finally, the output of $\hat{u}_{N,\theta}$ is the projection of \mathbf{z}_{N+1} by the local transformation \mathcal{Q} as (Li et al., 2020):

$$\hat{u}_{N,\theta} = \mathcal{Q} \left(\sum_{i=1}^{N+1} \left(\sum_{n=0}^{M-1} \mathbf{z}_i[n] \overline{\mathcal{B}_i(e^{i2\pi n/M}; a_{1:i})} \right) \odot \mathcal{B}_i \right). \quad (13)$$

4 PROPERTIES OF AFMO

Connections to AFD theory. Adaptive Fourier decomposition (AFD) is a novel signal decomposition technique that leverages the Takenaka-Malmquist system and adaptive orthogonal bases (Qian, 2010; Qian et al., 2012). It admits a proved convergence of any signal $s \in \mathcal{H}$ such that $s = \sum_{i=1}^{\infty} \langle s, \mathcal{B}_i \rangle \mathcal{B}_i$ (Qian et al., 2011; Wang et al., 2022) for the chosen orthonormal bases \mathcal{B}_i (Saitoh et al., 2016). Thus, the output of Equation 12 \mathbf{z}_{i+1} , is equivalent to the AFD operation, i.e., $\mathbf{z}_{i+1} = \sum_{k=1}^i \langle \mathbf{z}_k, \mathcal{B}_k \rangle \mathcal{B}_k$. Furthermore, the output in Equation 13 can be approximated as $\hat{u}_{N,\theta} = \mathcal{Q} \left(\sum_{i=1}^{N+1} \langle \mathbf{z}_i, \mathcal{B}_i \rangle \mathcal{B}_i \right) \approx \sum_{i=1}^{N+1} \langle \hat{u}_{i-1,\theta}, \mathcal{B}_i \rangle \mathcal{B}_i$, where $\hat{u}_{i-1,\theta} = \mathcal{Q}(\mathbf{z}_i)$. This is also equivalent to the AFD operation. Thus, several theoretical properties of AFMO, including convergence and error bound (see theorems and proofs in Appendix D), can be guaranteed with efficiently large layers, thanks to AFMO's deep connections with AFD theory.

270 **Connections to Parnichkun et al. (2024).** Parnichkun et al. (2024) proposed a state-free inference
 271 of SSMs by learning the coefficients of the rational transfer function H instead of the traditional
 272 state-space matrices A , B , and C (Gu & Dao, 2023), which is called rational transfer function (RTF)
 273 approach. Specifically, the RTF learns H as:

$$274 \quad H(z) = h_0 + \frac{b_1 z^{-1} + b_2 z^{-2} + \cdots + b_n z^{-n}}{1 + a_1 z^{-1} + a_2 z^{-2} + \cdots + a_n z^{-n}}, \quad (14)$$

277 where a_i , b_i , and h_0 are denominator coefficients, numerator coefficients, and feedthrough term,
 278 respectively. When it comes to AFMO, we push the formulation of transfer function in Equation 8
 279 and learn the rational transfer function by learning the poles $a_{1:n}$ (for n terms). In Appendix E, we
 280 show that our way of learning poles leads to a similar form of Equation 14 with n learned parameters
 281 (poles) as opposed to learning $2n + 1$ parameters in RTF.

282 **Computational complexity.** In terms of computational complexity, AFMO has an overall computational
 283 complexity of $\mathcal{O}(N(M \log M + MD)) + \mathcal{O}(N_s MD)$. The former is from the processing
 284 block, whereas the latter comes from \mathcal{P} and \mathcal{Q} . When M is treated as a constant with $M \ll N_s$ and
 285 a local decoder is used, the dominant cost reduces to $\mathcal{O}(N_s D) + \mathcal{O}(N M \log M)$. Consequently,
 286 the complexity grows linearly with the number of mesh points N_s . With mesh size fixed, it is
 287 approximately linear in the number of latent tokens M and the number of blocks N .

290 5 NUMERICAL EXPERIMENTS

292 To illustrate the effectiveness of AFMO, we conduct numerical experiments with multiple baseline
 293 neural operators on diverse datasets including three categories: (i) regular grids: 2-D Darcy flow
 294 equation and 2-D Navier-Stokes equation (Li et al., 2020), (ii) irregular geometries: plasticity,
 295 airfoil, pipe, and elasticity (Li et al., 2023), (iii) PDEs with singularities: European option pricing
 296 under the Black-Scholes equation, and 3-D Brusselator (reaction-diffusion) equation from Cao et al.
 297 (2024) (see Appendix B).

298 **Metric.** In the training and evaluation stage, we utilize relative L^2 error as the metric for accuracy
 299 for all problems:

$$300 \quad \text{Rel-}L^2 = \frac{1}{\mathcal{N}} \sum_{i=1}^{\mathcal{N}} \frac{\|\mathcal{G}_\theta(a_i) - \mathcal{G}(a_i)\|_{L^2}}{\|\mathcal{G}(a_i)\|_{L^2}}, \quad (15)$$

303 where \mathcal{N} denotes the number of samples. We also consider training time, the number of parameters,
 304 and/or GPU memory usage as metrics for computational efficiency.

306 **Implementation details.** For baselines, we follow the implementation settings of their works.
 307 Note that the architecture of FNO (Li et al., 2020) has been updated after publication, we evaluate
 308 FNO using the newest architecture. For AFMO, we train 500 epochs on all datasets. We use AdamW
 309 optimizer with decoupled weight decay 1×10^{-5} , base learning rate 2×10^{-4} , and a cosine decay
 310 schedule (Loshchilov & Hutter, 2017) with a linear warm-up over the first 10% of total steps. The
 311 nonlinearity is GELU inside the processing blocks. We clip global grad-norm at 0.5 each step. Un-
 312 less stated otherwise, we use batch size 16, latent width 128, 64 latent tokens, 32 adaptive poles, and
 313 4 processing blocks with SSM state size 16, depthwise 1-D convolution (per channel) of kernel size
 314 4, channel expansion ratio 2. Experiments are conducted on a Linux workstation running Ubuntu
 315 (kernel 6.14, glibc 2.39) with Python 3.13.5 (Anaconda), PyTorch 2.8.0+cu129 (CUDA 12.9), an
 316 AMD Ryzen 9 9950X (16-core) processor, and a single NVIDIA GeForce RTX 4090 (48 GB) GPU.
 317 CUDA is enabled.

318 5.1 NUMERICAL RESULTS OF BENCHMARK DATASETS

320 Table 1 shows the comprehensive comparison with various baselines on the six benchmark problems.
 321 Among those problems, N-S and Darcy flow datasets apply regular grids, elasticity dataset uses point
 322 clouds, whereas others are generated under structured meshes (Li et al., 2020; 2023). AFMO con-
 323 sistently outperforms existing SOTA models by an average improvement of 28.42%. In particular,
 for airfoil, Darcy, and N-S datasets, the relative L^2 error decreased more than 30% compared to

the existing SOTA models, demonstrating the superior performance of AFMO compared to existing frequency-, transformer-, and Mamba-based models when solving complex dynamics and handling irregular geometries. To solve the complex dynamics, Tiwari et al. (2025) incorporates latent representations and SSMs, which can be considered as integral kernels without orthogonality. Meanwhile, ONO (Xiao et al., 2023b) uses an orthogonal attention to ensure orthogonality. Numerical results on irregular geometries, including elasticity ($0.0050 \rightarrow 0.0043$), plasticity ($0.0007 \rightarrow 0.0006$), airfoil ($0.0041 \rightarrow 0.0020$), and pipe ($0.0026 \rightarrow 0.0023$), show that the systematic integration of orthonormal kernels and SSMs leads to an exact AFD approximation and in turn improves PDE solution accuracy in irregular geometries.

Table 1: Relative L^2 error comparisons of AFMO with baselines across six benchmark datasets. Lower relative L^2 error is better. We quantify the improvement as the gain of AFMO relative to the L^2 error of the second best model. **Bold** means the best model, underline means the second best model, **red** means the third best model, and **blue** means the fourth best model.

Models	Elasticity	Plasticity	Airfoil	Pipe	N-S	Darcy
FNO (Li et al., 2020)	0.0229	0.0074	0.0138	0.0067	<u>0.0417</u>	0.0052
U-FNO (Wen et al., 2022)	0.0239	0.0039	0.0269	0.0056	0.2231	0.0183
F-FNO (Tran et al., 2021)	0.0263	0.0047	0.0078	0.0070	0.2322	0.0077
LNO (Wang & Wang, 2024)	0.0052	0.0029	0.0051	<u>0.0026</u>	0.0845	0.0049
ONO (Xiao et al., 2023b)	0.0118	0.0048	0.0061	0.0052	0.1195	0.0076
WMT (Gupta et al., 2021)	0.0359	0.0076	0.0075	0.0077	0.1541	0.0082
Galerkin (Cao, 2021)	0.0240	0.0120	0.0118	0.0098	0.1401	0.0084
LSM (Wu et al., 2023)	0.0218	0.0025	0.0059	0.0050	0.1535	0.0065
OFormer (Li et al., 2022)	0.0183	0.0017	0.0183	0.0168	0.1705	0.0124
Transolver (Wu et al., 2024)	0.0062	0.0013	0.0053	0.0047	0.0879	0.0059
Transolver++ (Luo et al., 2025)	0.0064	0.0014	0.0051	0.0027	0.1010	0.0089
LaMO (Tiwari et al., 2025)	<u>0.0050</u>	<u>0.0007</u>	<u>0.0041</u>	<u>0.0038</u>	0.0460	0.0039
AFMO (ours)	0.0043	0.0006	0.0020	0.0023	0.0278	0.0021
Improvement	14.0%	14.3%	51.2%	11.5%	33.3%	46.2%

Computational Efficiency. To explore the computational efficiency of AFMO, we focus on Darcy and airfoil problems. On average, AFMO reaches 46.2% and 51.2% reduction in training time over SOTA models in these two problems, as shown in Figure 1. With light architectures and small GPU memory, AFMO achieves the best training speed. Compared to the SOTA neural operator, LaMO (Tiwari et al., 2025), AFMO is $\sim 1.2 \times$ faster and $\sim 2.5 \times$ lighter with similar GPU memory. Instead of using orthogonal attention as in ONO (Xiao et al., 2023b), AFMO employs bases in the orthogonal form (Equation 6), which does not require an orthogonalization process, thereby saving $\sim 2.7 \times$ in training time and $\sim 3 \times$ in GPU memory compared to ONO.

Scalability. We examine the computational scalability of AFMO on 2-D Darcy flow problem. From Table 2, we observe that, as the grid dimension changes from 64 to 128 (N_s becomes 4 times larger), both training and inference times increase approximately linearly (by about 4 times), which aligns with the computational complexity result mentioned earlier. The memory usage remains relatively constant with only a slight increase. This reflects the architectural characteristics of AFMO, where the main computations (SSM blocks) are performed on M latent tokens rather than on N_s physical points, and thus the memory footprint is largely decoupled from the input resolution N_s .

Table 2: AFMO is computationally scalable with respect to input resolution N_s .

Grid dimensions	Grid size N_s	Training time (sec/epoch)	Inference time (sec/epoch)	GPU memory (GB)
64 \times 64	4096	14.0	0.007	2.3
128 \times 128	16384	52.5	0.28	2.4
256 \times 256	65536	205.0	1.12	2.7

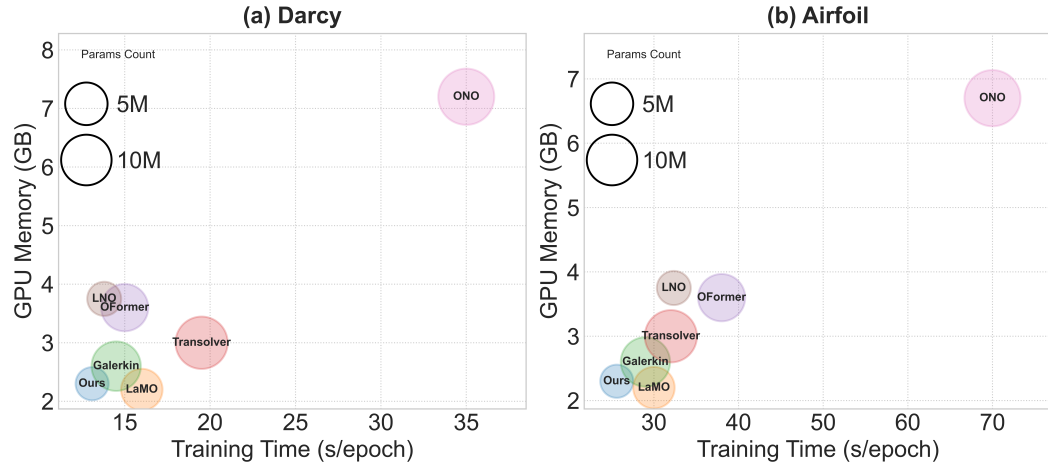
378 **Learned pole distributions across layers.** To understand how the adaptive poles are selected
 379 and evolved, Figure showcases the distributions per layer for 2-D Darcy flow and 3-D Brusselator
 380 equations. The learned poles of AFMO on Darcy flow problem tend to approach to the boundary of
 381 the unit disk, while those on the Brusselator problem tend to be in the interior of the unit disk. The
 382 reason is that, the challenging characteristics and singularities of the Darcy flow problem are located
 383 at the boundaries, and then more adaptive poles would be put there. Meanwhile, the complexity of
 384 the Brusselator problem does not come from the boundaries. It comes from the local, non-linear
 385 reaction that happens at every single point inside the domain. Therefore, most of the learned poles
 386 should be put inside the unit disk.

387 5.2 EUROPEAN OPTIONS PRICING

389 To demonstrate the versatility of AFMO in solving different PDEs in different contexts, we consider
 390 the European calls/puts problem modeled using the Black–Scholes equation with continuous divi-
 391 dend yield q . For contract/market parameters $(r, \sigma, q, K, T, \text{is_call})$, the price $V(S, t)$ satisfies
 392 the Black–Scholes equation (Barles & Soner, 1998):

$$393 \partial_t V + \frac{1}{2} \sigma^2 S^2 \partial_{SS} V + (r - q)S \partial_S V - rV = 0, \quad S \in [S_{\min}, S_{\max}], \quad t \in [0, T], \quad (16)$$

395 with terminal payoff $V(S, T) = \max(\pm(S - K), 0)$ (+ sign for calls, – for puts) and the linear
 396 boundary conditions $V(0, t) = 0$ for calls, $V(0, t) = Ke^{-r(T-t)}$ for puts, and controlled growth
 397 as $S \rightarrow \infty$. This problem setting leads to two singular features: (i) the terminal payoff kink at
 398 $S = K$ (jump in $\partial_S V$, concentration in $\partial_{SS} V$) as $t_{\text{norm}} \uparrow 1$; and (ii) degeneracy near small S as
 399 a result of the $S^2 \partial_{SS} V$ diffusion term. Our goal is to learn the operator that maps the parameters
 400 $(r, \sigma, q, K, T, \text{is_call})$ to the price $V(S, t)$. By comparing AFMO with a set of top-performing
 401 solvers, we observe from Table 3 that average improvements of 25%, 4.1%, and 52.7% have been
 402 achieved by AFMO in terms of relative L^2 error, training time, and parameter counts, respectively.
 403 This indicates that AFMO can accurately and efficiently solve PDE problems with singular features.



420 Figure 1: Comparisons of training time per epoch, number of parameters, and GPU memory among
 421 existing SOTA models on (a) Darcy and (b) airfoil, where AFMO exhibits the strongest incremental
 422 gains.

423 5.3 ABLATION STUDIES

426 **Adaptive kernels vs. static kernels.** We now consider the need and benefits of using adaptive
 427 kernels. A kernel is adaptive when its parameterization (e.g., coefficients) varies with the input. In
 428 this work, the formulation of Equation 6 varies with the learned poles $a_{1:i}$ and thus is an adaptive
 429 kernel. We also randomly fix the value of $a_{1:i}$ for static kernels for comparison. Furthermore,
 430 although a total of i poles are needed for i -th processing block, one can still identify more poles
 431 and select the best i poles for implementation. Table 4 shows the relative L^2 error results across six
 benchmark datasets and the European options (EO) dataset. We find that, using adaptive kernels, the

432 Table 3: European option pricing: relative L^2 error and resource profile. Lower is better for error,
 433 GPU memory, and training time. Parameter counts shown in millions. **Bold** = best, underline =
 434 second best, and **red** = third best.

436 Models	437 Rel. L^2 (\downarrow)	438 Training Time (sec/epoch, \downarrow)	439 Params (M, \downarrow)
FNO (Li et al., 2020)	0.0016	25.1	3.78
LNO (Wang & Wang, 2024)	0.0010	<u>21.7</u>	<u>2.56</u>
Transolver (Wu et al., 2024)	0.0012	<u>22.3</u>	5.91
LAMO (Tiwari et al., 2025)	<u>0.0008</u>	22.5	3.52
AFMO (ours)	0.0006	20.8	1.21

444 relative L^2 errors reduce significantly compared to using static poles for all benchmark problems
 445 considered. In fact, the relative L^2 errors when selecting only 4 poles are lower than those when
 446 selecting 32 static poles.

447 Table 4: Relative L^2 error comparisons for **Static** vs. **Adaptive** kernels across seven benchmarks.
 448 Lower is better.

450 Models	451 Number of poles	452 Elasticity	453 Plasticity	454 Airfoil	455 Pipe	456 N-S	457 Darcy	458 EO
AFMO (static)	32	0.0097	0.0021	0.0067	0.0072	0.1103	0.0174	0.0035
	4	0.0056	0.0012	0.0033	0.0029	0.0311	0.0057	0.0014
	6	0.0051	0.0010	0.0031	0.0027	0.0298	0.0047	0.0010
	8	0.0049	0.0008	0.0027	0.0025	0.0281	0.0036	0.0009
	16	0.0046	0.0008	0.0023	0.0028	0.0290	0.0029	0.0008
	32	0.0043	0.0006	0.0020	0.0023	0.0278	0.0021	0.0006
	64	0.0048	0.0007	0.0036	0.0031	0.0372	0.0046	0.0009

460 **Need for ensuring orthogonality.** To understand how orthogonal kernels affect AFMO performance,
 461 we conduct another ablation study by using non-orthogonal kernels (i.e., Equation 5)
 462 in the AFMO framework. In this case, the transfer functions used in SSMs are $H_i(e^{i\omega}) =$
 463 $(1 - |a_i|^2) \sum_{n=0}^{\infty} (\bar{a}_i)^n e^{in\omega}$ to match the output of AFD operation. Without orthogonality, AFMO
 464 experiences higher relative L^2 error, especially for problems with irregular geometries (e.g., airfoil
 465 0.0020 \rightarrow 0.0083 and elasticity 0.0043 \rightarrow 0.0094). At the same time, the training time also in-
 466 creases by $\sim 50.3\%$ per epoch on average across all six benchmark datasets. This shows that the use
 467 of orthogonal kernels (i.e., TM systems) helps improve both accuracy and computational efficiency
 468 of AFMO solver.

469 **Choice of SSMs.** Finally, we evaluate the choice of bidirectional SSMs in AFMO compared to
 470 unidirectional SSMs and multidirectional SSMs. Results in Figure 2 indicate that the choice of
 471 bidirectional SSMs in AFMO consistently outperforms other two SSMs in all datasets.

475 5.4 EXPERIMENT USING REAL-WORLD NOISY DATASET

476 To validate AFMO’s performance on noisy real-world datasets, we perform experiments using the
 477 latex glove DIC (Digital Image Correlation) original dataset (You et al., 2022). The goal is to learn
 478 the mechanical response of a nitrile glove sample directly from experimental data, without assuming
 479 a known constitutive law. The goal is to predict the displacement field at the current loading step.
 480 The input includes the spatial coordinates, the displacement field from the previous step, and the
 481 current boundary displacement. We compare the performance of AFMO to the current SOTA of this
 482 dataset, IFNO, as well as FNO as follows. To ensure fair comparison, we conduct experiments using
 483 the same settings as IFNO with the number of hidden layers ranging from 3 to 12.

484 In addition, You et al. (2022) also reported the results of generalized Mooney-Rivlin (GMR) model
 485 in two settings. The relative L^2 errors of GMR model fitting and GMR inverse analysis are 3.30E-01

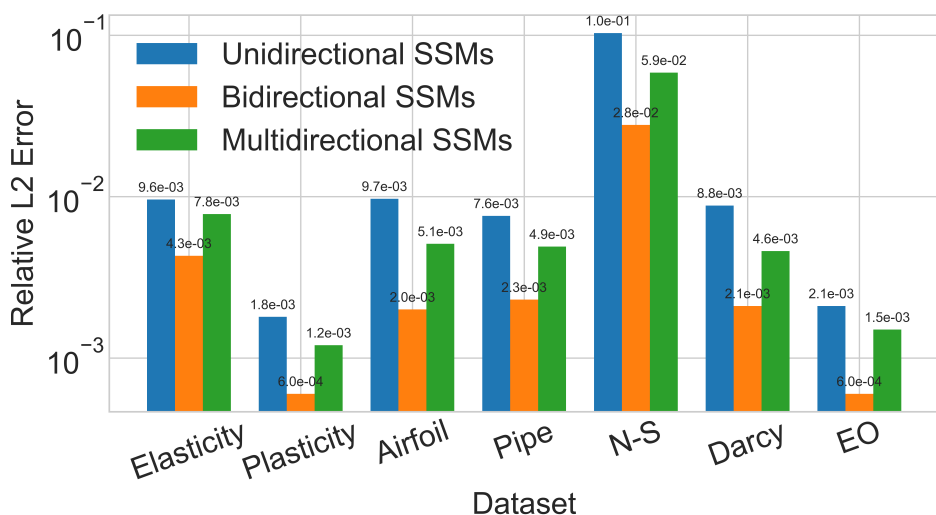


Figure 2: Contribution of three SSMs across seven benchmark datasets. Note that we do not apply weights shared for all experiments. Lower is better.

Table 5: Relative L^2 error of AFMO and other baselines using the latex glove DIC (Digital Image Correlation) original dataset.

Number of hidden layers	AFMO	IFNO	FNO
3	2.87E-02 \pm 4.29E-04	3.43E-02 \pm 4.96E-04	3.40E-02 \pm 4.09E-04
6	2.50E-02 \pm 3.28E-04	3.34E-02 \pm 4.53E-04	3.84E-02 \pm 4.21E-04
12	2.32E-02 \pm 4.20E-04	3.32E-02 \pm 4.41E-04	4.66E-02 \pm 1.47E-03

and 2.91E-01, respectively. We can observe that our AFMO consistently outperforms other models in every L . Finally, the best reported result of IFNO is 3.30E-02 \pm 4.63E-04 when $L = 24$ (You et al., 2022). Although we do not conduct the experiment $L = 24$ due to the limited time, our AFMO still performs better than the best result of IFNO.

6 CONCLUSIONS

In this paper, we propose a novel neural operator AFMO for solving nonlinear PDEs on irregular geometries and singularities. AFMO maps the physical tokens in an RKHS where the global spectral transform and data-dependent orthogonal kernels are incorporated. By conducting a tailored design of the TM layer and SSM block fully guided by the AFD theory, we show that the output of AFMO exactly matches with AFD operation, hence offering rigorous convergence guarantee and other desirable properties. We show that the novel architecture of AFMO enables its outstanding performance compared to existing SOTA neural operators in a series of physical and financial benchmark problems.

7 REPRODUCIBILITY STATEMENT

All code and datasets have been either made publicly available in an anonymous repository or as a part of supplementary material to facilitate replication and verification. The experimental setup, including training steps, model configurations, and hardware details, is described in detail in the paper. We have also provided a full description of implementation details, to assist others in reproducing our experiments. Additionally, six benchmark datasets, such as pipe, are publicly available, ensuring consistent and reproducible evaluation results.

540 REFERENCES
541

542 Guy Barles and Halil Mete Soner. Option pricing with transaction costs and a nonlinear Black-
543 Scholes equation. *Finance and Stochastics*, 2(4):369–397, 1998.

544 Qianying Cao, Somdatta Goswami, and George Em Karniadakis. Laplace neural operator for solving
545 differential equations. *Nature Machine Intelligence*, 6(6):631–640, 2024.

546 Shuhao Cao. Choose a transformer: Fourier or galerkin. *Advances in neural information processing
548 systems*, 34:24924–24940, 2021.

549 Gengxiang Chen, Xu Liu, Qinglu Meng, Lu Chen, Changqing Liu, and Yingguang Li. Learning
550 neural operators on Riemannian manifolds. *National Science Open*, 3(6):20240001, 2024.

551 Chun-Wun Cheng, Jiahao Huang, Yi Zhang, Guang Yang, Carola-Bibiane Schönlieb, and Angelica I
553 Aviles-Rivero. Mamba neural operator: Who wins? transformers vs. state-space models for pdes.
554 *arXiv preprint arXiv:2410.02113*, 2024.

555 Vladimir Sergeevich Fanaskov and Ivan V Oseledets. Spectral neural operators. In *Doklady Math-
556 ematics*, volume 108, pp. S226–S232. Springer, 2023.

557 Albert Gu and Tri Dao. Mamba: Linear-time sequence modeling with selective state spaces. *arXiv
559 preprint arXiv:2312.00752*, 2023.

560 Albert Gu, Karan Goel, and Christopher Ré. Efficiently modeling long sequences with structured
561 state spaces. *arXiv preprint arXiv:2111.00396*, 2021.

562 John Guibas, Morteza Mardani, Zongyi Li, Andrew Tao, Anima Anandkumar, and Bryan Catan-
563 zaro. Adaptive Fourier neural operators: Efficient token mixers for transformers. *arXiv preprint
564 arXiv:2111.13587*, 2021.

565 Gaurav Gupta, Xiongye Xiao, and Paul Bogdan. Multiwavelet-based operator learning for differen-
566 tial equations. *Advances in Neural Information Processing Systems*, 34:24048–24062, 2021.

567 Gaurav Gupta, Xiongye Xiao, Radu Balan, and Paul Bogdan. Non-linear operator approximations
568 for initial value problems. In *International Conference on Learning Representations (ICLR)*,
569 2022.

570 Zheyuan Hu, Nazanin Ahmadi Daryakenari, Qianli Shen, Kenji Kawaguchi, and George Em Kar-
571 niadakis. State-space models are accurate and efficient neural operators for dynamical systems.
572 *arXiv preprint arXiv:2409.03231*, 2024.

573 Zijie Li, Kazem Meidani, and Amir Barati Farimani. Transformer for partial differential equations'
574 operator learning. *arXiv preprint arXiv:2205.13671*, 2022.

575 Zongyi Li, Nikola Kovachki, Kamyar Azizzadenesheli, Burigede Liu, Kaushik Bhattacharya, An-
576 drew Stuart, and Anima Anandkumar. Fourier neural operator for parametric partial differential
577 equations. *arXiv preprint arXiv:2010.08895*, 2020.

578 Zongyi Li, Daniel Zhengyu Huang, Burigede Liu, and Anima Anandkumar. Fourier neural oper-
579 ator with learned deformations for PDEs on general geometries. *Journal of Machine Learning
580 Research*, 24(388):1–26, 2023.

581 Levi Lingsch, Mike Y Michelis, Emmanuel De Bézenac, Sirani M Perera, Robert K Katschmann,
582 and Siddhartha Mishra. Beyond regular grids: Fourier-based neural operators on arbitrary do-
583 mains. *arXiv preprint arXiv:2305.19663*, 2023.

584 Ilya Loshchilov and Frank Hutter. Decoupled weight decay regularization. *arXiv preprint
585 arXiv:1711.05101*, 2017.

586 Huakun Luo, Haixu Wu, Hang Zhou, Lanxiang Xing, Yichen Di, Jianmin Wang, and Mingsheng
587 Long. Transolver++: An accurate neural solver for pdes on million-scale geometries, 2025. URL
588 <https://arxiv.org/abs/2502.02414>.

594 Rom N Parnichkun, Stefano Massaroli, Alessandro Moro, Jimmy TH Smith, Ramin Hasani, Mathias
595 Lechner, Qi An, Christopher Ré, Hajime Asama, Stefano Ermon, et al. State-free inference of
596 state-space models: The transfer function approach. *arXiv preprint arXiv:2405.06147*, 2024.

597

598 Tao Qian. Intrinsic mono-component decomposition of functions: an advance of Fourier theory.
599 *Mathematical Methods in the Applied Sciences*, 33(7):880–891, 2010.

600 Tao Qian, Liming Zhang, and Zhixiong Li. Algorithm of adaptive fourier decomposition. *IEEE*
601 *Transactions on Signal Processing*, 59(12):5899–5906, 2011.

602 Tao Qian, Wolfgang Sprößig, and Jinxun Wang. Adaptive Fourier decomposition of functions in
603 quaternionic Hardy spaces. *Mathematical Methods in the Applied Sciences*, 35(1):43–64, 2012.

604

605 Md Ashiqur Rahman, Zachary E Ross, and Kamyar Azizzadenesheli. U-no: U-shaped neural oper-
606 ators. *arXiv preprint arXiv:2204.11127*, 2022.

607

608 Saburou Saitoh, Yoshihiro Sawano, et al. *Theory of reproducing kernels and applications*, vol-
609 ume 44. Springer, 2016.

610 Karn Tiwari, Niladri Dutta, NM Krishnan, et al. Latent mamba operator for partial differential
611 equations. *International Conference on Machine Learning*, 2025.

612

613 Alasdair Tran, Alexander Mathews, Lexing Xie, and Cheng Soon Ong. Factorized fourier neural
614 operators. *arXiv preprint arXiv:2111.13802*, 2021.

615

616 Tapas Tripura and Souvik Chakraborty. Wavelet neural operator for solving parametric partial differ-
617 ential equations in computational mechanics problems. *Computer Methods in Applied Mechanics
618 and Engineering*, 404:115783, 2023.

619

620 Tian Wang and Chuang Wang. Latent neural operator for solving forward and inverse pde problems.
621 *Advances in Neural Information Processing Systems*, 37:33085–33107, 2024.

622

623 Ze Wang, Chi Man Wong, Agostinho Rosa, Tao Qian, and Feng Wan. Adaptive fourier decom-
624 position for multi-channel signal analysis. *IEEE Transactions on Signal Processing*, 70:903–918,
625 2022.

626

627 Gege Wen, Zongyi Li, Kamyar Azizzadenesheli, Anima Anandkumar, and Sally M Benson. U-
628 fno—an enhanced fourier neural operator-based deep-learning model for multiphase flow. *Ad-
629 vances in Water Resources*, 163:104180, 2022.

630

631 Haixu Wu, Tengge Hu, Huakun Luo, Jianmin Wang, and Mingsheng Long. Solving high-
632 dimensional PDEs with latent spectral models. *arXiv preprint arXiv:2301.12664*, 2023.

633

634 Haixu Wu, Huakun Luo, Haowen Wang, Jianmin Wang, and Mingsheng Long. Transolver: A fast
635 transformer solver for pdes on general geometries. *arXiv preprint arXiv:2402.02366*, 2024.

636

637 Xiongye Xiao, Defu Cao, Ruochen Yang, Gaurav Gupta, Gengshuo Liu, Chenzhong Yin, Radu
638 Balan, and Paul Bogdan. Coupled multiwavelet neural operator learning for coupled partial dif-
639 fferential equations. *arXiv preprint arXiv:2303.02304*, 2023a.

640

641 Zipeng Xiao, Zhongkai Hao, Bokai Lin, Zhijie Deng, and Hang Su. Improved operator learning by
642 orthogonal attention. *arXiv preprint arXiv:2310.12487*, 2023b.

643

644 Huaiqian You, Quinn Zhang, Colton J. Ross, Chung-Hao Lee, and Yue Yu. Learning deep implicit
645 fourier neural operators (ifnos) with applications to heterogeneous material modeling. *Computer
646 Methods in Applied Mechanics and Engineering*, 398:115296, 2022.

647

648 Yue Yu, Ning Liu, Fei Lu, Tian Gao, Siavash Jafarzadeh, and Stewart A Silling. Nonlocal attention
649 operator: Materializing hidden knowledge towards interpretable physics discovery. *Advances in
650 Neural Information Processing Systems*, 37:113797–113822, 2024.

651

652 Jianwei Zheng, Wei Li, Ni Xu, Junwei Zhu, and Xiaoqin Zhang. Alias-free mamba neural operator.
653 *Advances in Neural Information Processing Systems*, 37:52962–52995, 2024.

648 A NOTATION LIST
649

650	a	Parameter function (input)
651	$\hat{u}_{N,\theta}$	Output of AFMO with N blocks and parameters θ
652	N	Number of processing blocks
653	N_s	Number of input physical tokens
654	M	Number of encoded latent tokens ($M \ll N_s$)
655	D_{embed}	Embedding dimension of latent tokens
656	\mathbf{x}_{phys}	Input physical features
657	\mathbf{g}_{phys}	Positional embedding of coordinates
658	\mathbf{z}_i	Token representation after the i -th block
659	\mathbf{z}_0	Encoded tokens produced by the lifting operator \mathcal{P}
660	\mathbf{z}_1	Tokens mapped into RKHS by operator \mathcal{R}
661	\mathcal{P}	Lifting operator mapping physical tokens to encoded tokens
662	\mathcal{Q}	Projection operator mapping latent tokens back to output space
663	\mathcal{R}	Mapping operator from latent tokens to RKHS
664	\mathcal{L}^i	Processing block at layer i ($\text{SSM}^i \circ \text{TM}^i$)
665	\mathcal{S}^i	Aggregation operator with skip connections at block i
666	TM^i	TM layer performing spectral transform via TM bases
667	SSM^i	Bidirectional SSM block parameterized by transfer function
668	$\mathcal{B}_i(z; a_{1:i})$	i -th TM basis generated by poles $a_{1:i}$
669	$a_{1:i}$	Set of learned poles $\{a_1, \dots, a_i\}$ in the unit disk \mathbb{D}
670	$K_a(z)$	Reproducing kernel $\frac{1}{1-\bar{a}z}$
671	$H_i(e^{i\omega})$	Transfer function of the i -th SSM block
672	$h_i[n]$	Impulse response of the i -th SSM block
673	$\langle x, f \rangle$	Inner product $\frac{1}{\tilde{N}} \sum_{n=0}^{\tilde{N}-1} x[n] \overline{f(e^{i2\pi n/\tilde{N}})}$
674	\odot	Element-wise (Hadamard) product
675	\mathcal{H}	Reproducing Kernel Hilbert Space (RKHS)
676	\tilde{N}	Length of signal in inner product definition

688
689 B ILLUSTRATIVE EXAMPLES690
691
692 **1-D advection PDE with high-frequency perturbation.** We evaluate LaMO on a 1-D linear advection benchmark governed by
693

694
695
$$u_t + c u_x = 0 \tag{17}$$

696

697 on a periodic unit interval. Initial conditions $u_0(x)$ are synthesized as smooth Fourier mixtures
698 $\sum_{k=1}^{k_{\max}} a_k \sin(2\pi kx + \phi_k)$ with amplitudes decaying as $a_k \sim (1+k)^{-1}$, to which we add a weak
699 high-frequency spike at wavenumber k_{hi} to probe aliasing and phase accuracy. Trajectories are
700 advanced to time T with a conservative first-order upwind scheme at Courant number $\text{CFL} = c\Delta t/\Delta x \leq 0.5$, ensuring stability while preserving sharp phase relationships; the target is the
701 advected field $u(\cdot, T)$.

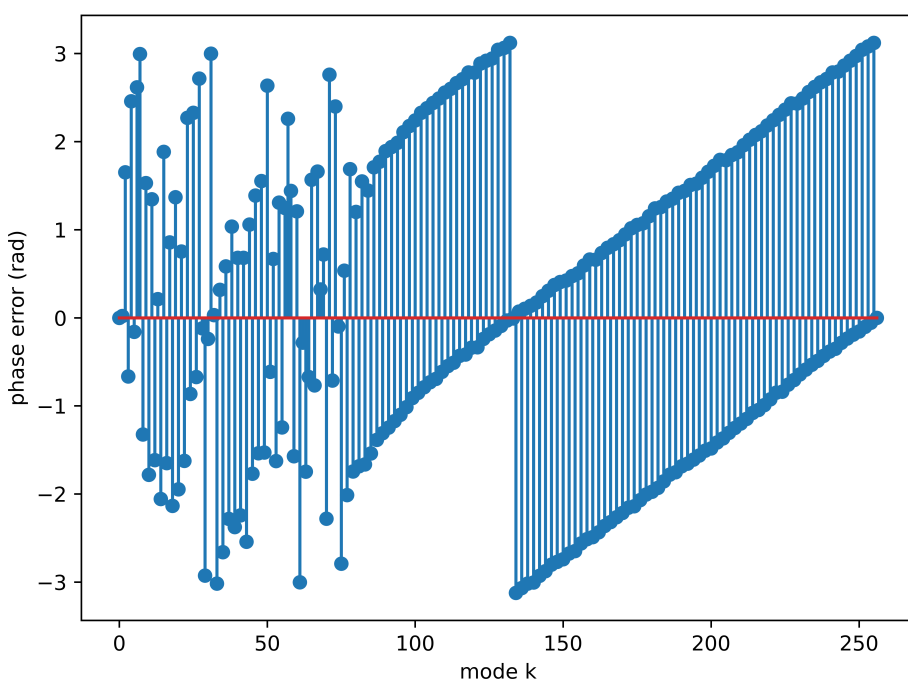


Figure 3: Phase error of solutions predicted by LaMO.

Figure 3 visualizes the phase error of LaMO’s predictions, revealing a pronounced degradation for high-frequency modes (approximately $k \in [140, 250]$). This suggests that LaMO struggles to faithfully capture phase at the upper end of the spectrum.

2-D Darcy flow equation with fractal noise. We construct a challenging 2-D Darcy dataset by solving

$$-\nabla \cdot (k(x, y) \nabla u(x, y)) = f(x, y) \quad (18)$$

on $[0, 1]^2$ with homogeneous Dirichlet boundaries, where the permeability k is positive, highly heterogeneous, and fractal-like. Specifically, k is generated by exponentiating a band-limited fractional Gaussian field (small Hurst parameter for roughness) and then modulating it with narrow channel masks and inclusions to induce strong anisotropy and high contrast. The forcing f combines a weak background term with several randomized Gaussian sources/sinks, which produce near-singular behavior in the solution. The variable-coefficient elliptic problem is discretized on a Cartesian grid using a flux-conservative 5-point stencil with harmonic averaging of k , and solved to tight tolerance via conjugate gradients. For learning, each sample is subsampled irregularly: we draw P points $\{(x_i, y_i)\}$ and record $u(x_i, y_i)$, yielding pairs (X, Y, U) without exposing k or f .

To visualize and stress singular structures, we show in Figure 4 (a) and (c): (i) contours of the potential u highlighting global flow topology, and (ii) a logarithmic map of the gradient magnitude, $\log |\nabla u|$, computed on a reconstructed dense grid via triangulation. Figure 4 shows LAMO cannot capture the singularities of u and $\log |\nabla u|$. Furthermore, once the complex singularities appear, the performance of LAMO will be affected.

3-D Brusselator problem. We introduce a new 3-D Brusselator (diffusion-reaction equation) problem using the dataset from Laplace neural operator (LNO) (Cao et al., 2024). The Brusselator problem is formulated as:

$$D \frac{\partial^2 y}{\partial x^2} + ky^2 - \frac{\partial y}{\partial t} = f(x, t), \quad (19)$$

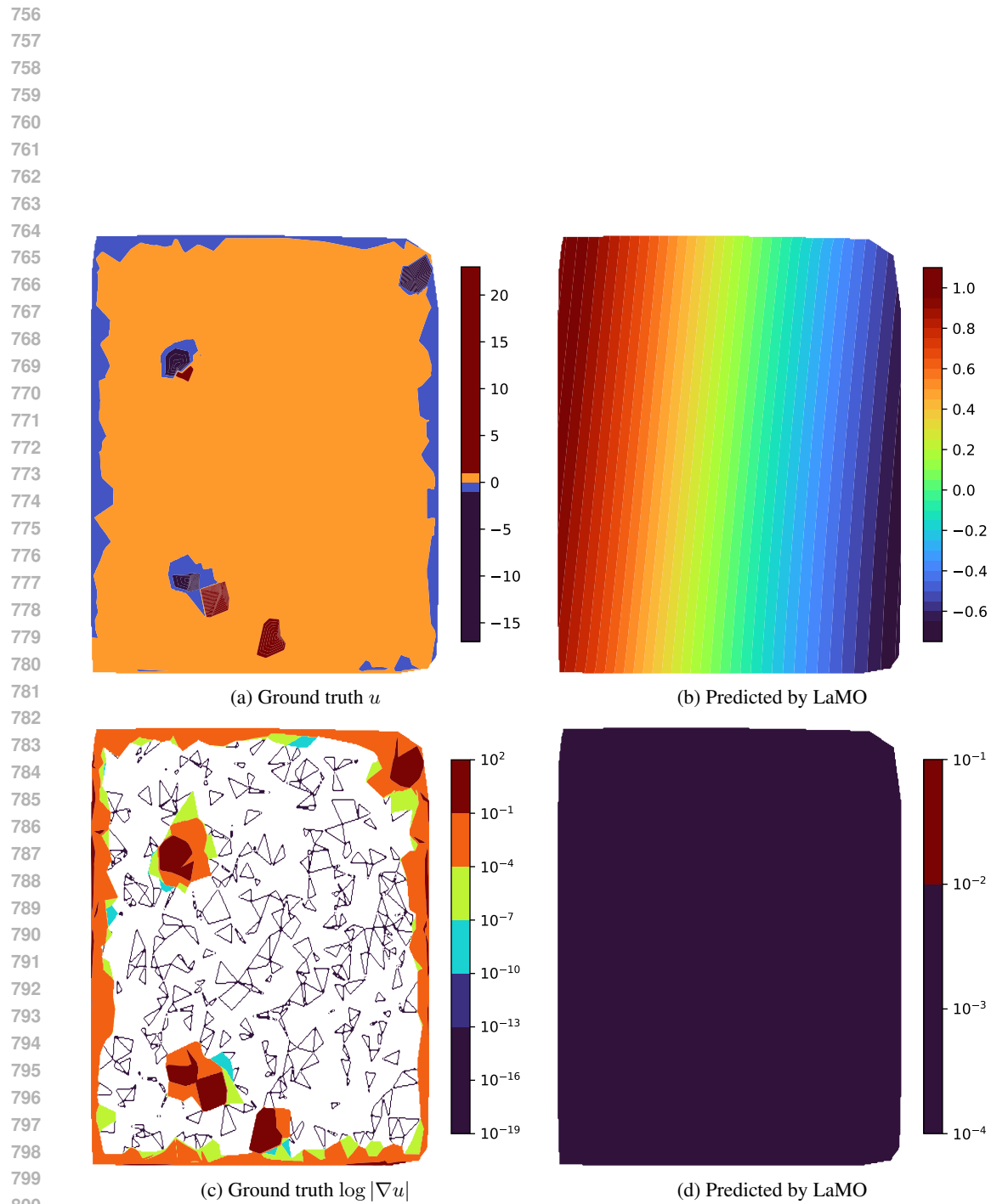


Figure 4: The predicted results produced by LaMO compared to the ground truth.

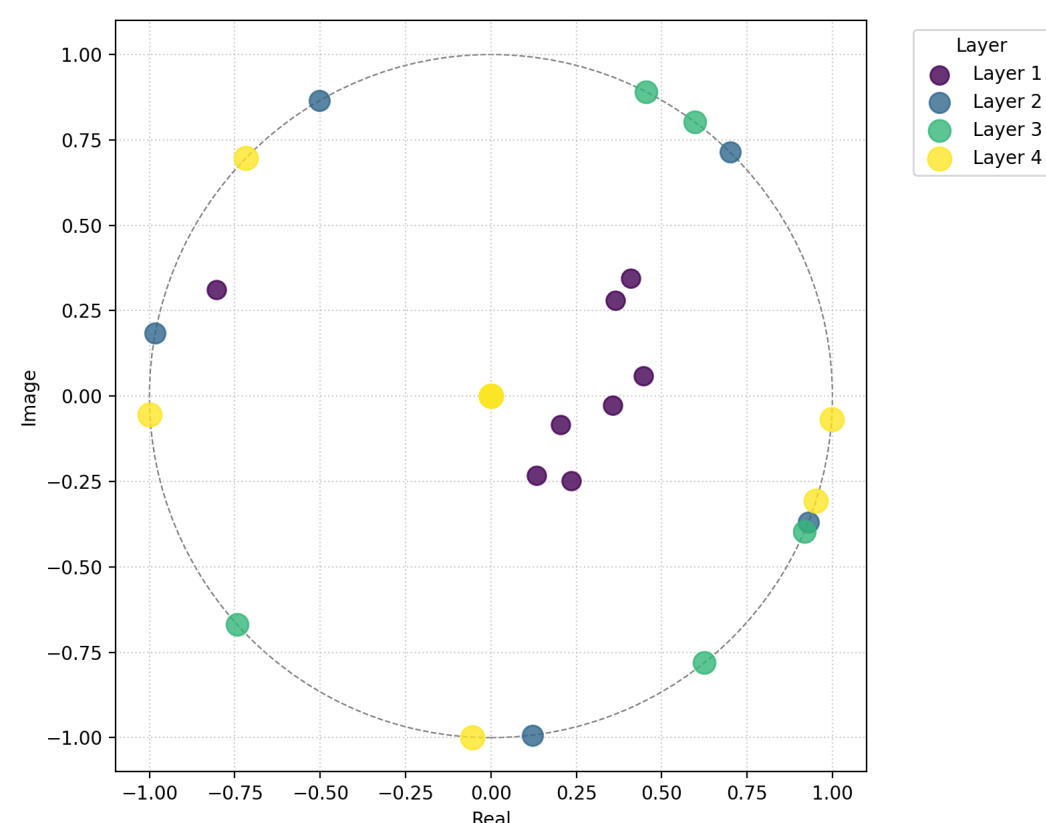


Figure 5: Learned poles distribution for the 2-D Darcy flow equation.

where $y(x, t)$ represents the concentration of chemical substances or particles at location x and time t , $f(x, t)$ is the source term and A is the amplitude of the source term. In this problem, the diffusion coefficient, $D = 0.01$, and the reaction rate, $k = 0.01$.

C DISTRIBUTION OF SELECTED POLES REFLECTS PROBLEM CHARACTERISTICS

To understand how AFMO’s pole selection process is adaptive to the characteristics and nature of the problem, we illustrate the learned pole distributions for the 2-D Darcy flow problem and 3-D Brusselator problem in Figures 5. To clarify, here we give a brief overview of the visualization results: The distribution of selected poles for the 2-D Darcy flow problem is shown in Figures 5 and 6, respectively.

We observe that, across the layers, the learned poles of AFMO on Darcy flow problem tend to approach to the boundary of the unit disk, while those on the Brusselator problem tend to be in the interior of the unit disk. The reason is that, Darcy flow problem is an elliptic equation, which is a smoothing operator. Thus, even though the input coefficient (the permeability) is very rough and discontinuous, the solution inside the domain will be well-behaved. Therefore, the challenging characteristics and singularities of the Darcy flow problem are located at the boundaries, and then more adaptive poles would be put there. Meanwhile, the complexity of the Brusselator problem does not come from the boundaries. It comes from the local, non-linear reaction that happens at every single point inside the domain. Therefore, most of the learned poles should be put inside the unit disk.

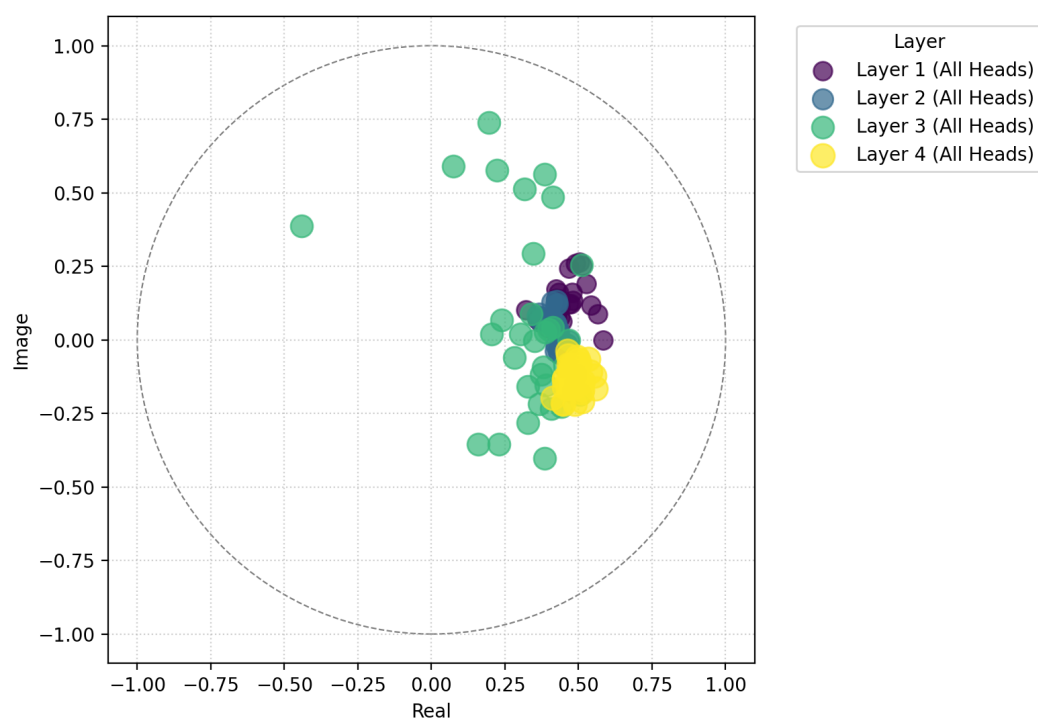


Figure 6: Learned poles distribution for the 3-D Brusselator equation.

D THEORETICAL RESULTS OF AFMO

Basic settings. Let $\mathbb{D} = \{z \in \mathbb{C} : |z| < 1\}$. Consider a reproducing kernel Hilbert space (RKHS) $(\mathcal{H}, \langle \cdot, \cdot \rangle_{\mathcal{H}})$ of complex-valued functions on \mathbb{D} with the following properties.

Assumption D.1. There is a family of normalized reproducing kernels $\{e_a : a \in \mathbb{D}\} \subset \mathcal{H}$ such that

$$e_a(z) = \frac{\sqrt{1 - |a|^2}}{1 - \bar{a}z} \in \mathcal{H}, \quad \langle f, e_a \rangle_{\mathcal{H}} = f(a) \sqrt{1 - |a|^2} \quad \forall f \in \mathcal{H}, a \in \mathbb{D}. \quad (20)$$

Given a pole sequence $a_{1:\infty} = (a_1, a_2, \dots) \subset \mathbb{D}$, define the Takenaka–Malmquist (TM) system by

$$\mathcal{B}_1(z) = e_{a_1}(z), \quad \mathcal{B}_i(z) = e_{a_i}(z) \prod_{j=1}^{i-1} \frac{z - a_j}{1 - \bar{a}_j z} \quad (i \geq 2). \quad (21)$$

Assume $\{\mathcal{B}_i\}_{i \geq 1}$ is an orthonormal system in \mathcal{H} , and its closed linear span equals the model space

$$K_B := \overline{\text{span}}\{\mathcal{B}_i : i \geq 1\} \subseteq \mathcal{H}, \quad (22)$$

where B is the Blaschke product with zeros $\{a_i\}$.

AFMO notation. Let $s \in \mathcal{H}$ be the latent target representation and $u^* = \mathcal{Q}(s)$, where $\mathcal{Q} : \mathcal{H} \rightarrow \mathcal{U}$ is a Lipschitz decoder with constant $L_{\mathcal{Q}}$. Define the ideal TM coefficients and partial sums

$$c_i^* := \langle s, \mathcal{B}_i \rangle_{\mathcal{H}}, \quad s_N := \sum_{i=1}^N c_i^* \mathcal{B}_i. \quad (23)$$

AFMO learns estimates \hat{c}_i of c_i^* (via an SSM in the frequency domain) and aggregates them through the skip connection:

$$z_{i+1} := z_i + \hat{c}_i \mathcal{B}_i, \quad z_1 := 0. \quad (24)$$

918 D.1 AGGREGATION IDENTITY AND FREQUENCY-DOMAIN COEFFICIENT EXTRACTION
919920 **Lemma D.2.** *Under 24, one has, for every $N \in \mathbb{N}$,*

921
922
$$z_{N+1} = \sum_{i=1}^N \widehat{c}_i \mathcal{B}_i. \quad (25)$$

923
924

925 *Proof.* The proof is by induction. For $N = 1$, $z_2 = z_1 + \widehat{c}_1 \mathcal{B}_1 = \widehat{c}_1 \mathcal{B}_1$, so 25 holds. Assume 25
926 holds for N , i.e., $z_{N+1} = \sum_{i=1}^N \widehat{c}_i \mathcal{B}_i$. Then
927

928
929
$$z_{N+2} = z_{N+1} + \widehat{c}_{N+1} \mathcal{B}_{N+1} = \sum_{i=1}^{N+1} \widehat{c}_i \mathcal{B}_i,$$

930

931 which establishes the claim for $N + 1$. □
932933 **Lemma D.3.** *Suppose the i -th SSM has transfer function*

934
935
$$H_i(e^{i\omega}) = \overline{\mathcal{B}_i(e^{i\omega})}, \quad (26)$$

936 *so that the block multiplies the input spectrum by $\overline{\mathcal{B}_i}$ and outputs the zero-lag correlation. If the
937 discrete inner product used by AFMO is a consistent quadrature for $\langle \cdot, \cdot \rangle_{\mathcal{H}}$ on the class $\{s\} \cup \{\mathcal{B}_i\}$,
938 then*

939
940
$$\widehat{c}_i \rightarrow \langle s, \mathcal{B}_i \rangle_{\mathcal{H}} = c_i^* \quad \text{as the quadrature is refined.} \quad (27)$$

941 *Proof.* By 26, the block forms (pointwise on the grid) $Y_i = \overline{\mathcal{B}_i} \cdot s$ in the transform domain; the zero-
942 lag correlation is the discretized inner product $\langle s, \mathcal{B}_i \rangle_{\text{disc}}$. Consistency of the quadrature implies
943 $\langle s, \mathcal{B}_i \rangle_{\text{disc}} \rightarrow \langle s, \mathcal{B}_i \rangle_{\mathcal{H}}$ as the grid is refined. Hence $\widehat{c}_i \rightarrow c_i^*$. □
944945 D.2 CONVERGENCE IN THE MODEL SPACE AND PROJECTION ERROR
946947 **Theorem D.4.** *Under Assumption D.1, if AFMO recovers the exact coefficients $c_i^* = \langle s, \mathcal{B}_i \rangle_{\mathcal{H}}$, then*

948
949
$$s_N := \sum_{i=1}^N c_i^* \mathcal{B}_i \xrightarrow[N \rightarrow \infty]{\mathcal{H}} \Pi_{K_B} s, \quad (28)$$

950
951

952 *the orthogonal projection of s onto K_B . Consequently,*

953
954
$$\|u^* - \mathcal{Q}(s_N)\| \leq L_{\mathcal{Q}} \|s - \Pi_{K_B} s\|_{\mathcal{H}} + L_{\mathcal{Q}} \|\Pi_{K_B} s - s_N\|_{\mathcal{H}} \xrightarrow[N \rightarrow \infty]{} L_{\mathcal{Q}} \text{dist}(s, K_B). \quad (29)$$

955

956 *Proof.* Because $\{\mathcal{B}_i\}$ is an orthonormal basis (ONB) of K_B , the Fourier expansion of $\Pi_{K_B} s$ in this
957 ONB has coefficients $\langle s, \mathcal{B}_i \rangle_{\mathcal{H}}$, and the N -th partial sum equals s_N . Convergence in norm to the
958 projection is standard for orthogonal series in a Hilbert space, giving 28. The bound 29 follows from
959 Lipschitz continuity of \mathcal{Q} :

960
961
$$\|u^* - \mathcal{Q}(s_N)\| = \|\mathcal{Q}(s) - \mathcal{Q}(s_N)\| \leq L_{\mathcal{Q}} \|s - s_N\| \leq L_{\mathcal{Q}} (\|s - \Pi_{K_B} s\| + \|\Pi_{K_B} s - s_N\|).$$

962 □963 *Remark.* No greedy or maximal selection is used. The MLP-generated poles determine K_B ; AFMO
964 converges to $\Pi_{K_B} s$, and to s whenever $s \in K_B$.
965966 D.3 BEST N -TERM ERROR AND RATES WITHOUT GREEDY SELECTION
967968 **Definition D.5.** Let $\mathcal{D} := \{\mathcal{B}_i(\cdot; a_{1:i}) : a_{1:i} \in \mathbb{D}^i, i \in \mathbb{N}\}$ be the TM dictionary. Define the best
969 N -term error
970

971
$$E_N(s) := \inf_{a_{1:N}, c_{1:N}} \left\| s - \sum_{i=1}^N c_i \mathcal{B}_i(\cdot; a_{1:i}) \right\|_{\mathcal{H}}. \quad (30)$$

972 **Theorem D.6.** Let $\tilde{a}_{1:N}$ be the poles output by the MLP and set $c_i^* = \langle s, \mathcal{B}_i(\cdot; \tilde{a}_{1:i}) \rangle_{\mathcal{H}}$. If AFMO
 973 learns \hat{c}_i , then
 974

$$975 \quad \left\| s - \sum_{i=1}^N \hat{c}_i \mathcal{B}_i(\cdot; \tilde{a}_{1:i}) \right\|_{\mathcal{H}} \leq E_N(s) + \Delta_{pole}(N) + \left(\sum_{i=1}^N |\hat{c}_i - c_i^*|^2 \right)^{\frac{1}{2}}, \quad (31)$$

978 where

$$979 \quad \Delta_{pole}(N) := \inf_{c_{1:N}} \left\| s - \sum_{i=1}^N c_i \mathcal{B}_i(\cdot; \tilde{a}_{1:i}) \right\|_{\mathcal{H}} - E_N(s) \geq 0. \quad (32)$$

982 *Proof.* Choose $a_{1:N}^{\text{best}}, c_{1:N}^{\text{best}}$ that attain (or ε -attain) $E_N(s)$ and denote $s_N^{\text{best}} :=$
 983 $\sum_{i=1}^N c_i^{\text{best}} \mathcal{B}_i(\cdot; a_{1:i}^{\text{best}})$. Then
 984

$$985 \quad \left\| s - \sum_{i=1}^N \hat{c}_i \mathcal{B}_i(\cdot; \tilde{a}_{1:i}) \right\| \leq \|s - s_N^{\text{best}}\| + \left\| s_N^{\text{best}} - \sum_{i=1}^N c_i^* \mathcal{B}_i(\cdot; \tilde{a}_{1:i}) \right\| + \left\| \sum_{i=1}^N (c_i^* - \hat{c}_i) \mathcal{B}_i(\cdot; \tilde{a}_{1:i}) \right\| \\ 986 \quad \leq E_N(s) + \Delta_{pole}(N) + \left(\sum_{i=1}^N |c_i^* - \hat{c}_i|^2 \right)^{1/2}.$$

991 The last inequality uses the definition of $\Delta_{pole}(N)$ and orthonormality of $\{\mathcal{B}_i(\cdot; \tilde{a}_{1:i})\}_{i=1}^N$. \square

993 **Corollary D.7.** Assume for the fixed MLP-produced poles $\tilde{a}_{1:i}$ that the exact TM coefficients satisfy
 994 the weak- ℓ^p decay

$$995 \quad |c_i^*|^* \leq C i^{-1/p}, \quad 0 < p < 2,$$

996 where $(|c_i^*|^*)$ is the nonincreasing rearrangement. Then

$$998 \quad \inf_{c_{1:N}} \left\| s - \sum_{i=1}^N c_i \mathcal{B}_i(\cdot; \tilde{a}_{1:i}) \right\|_{\mathcal{H}} = \mathcal{O}(N^{\frac{1}{2} - \frac{1}{p}}). \quad (33)$$

1001 If, in addition, $\Delta_{pole}(N) = o(1)$ and $(\sum_{i=1}^N |\hat{c}_i - c_i^*|^2)^{1/2} = o(1)$, then the AFMO error in 31 is
 1002 $\mathcal{O}(N^{\frac{1}{2} - \frac{1}{p}})$.
 1003

1004 *Proof.* For an orthonormal system, the best N -term error equals the ℓ^2 tail of the rearranged coefficients. With $|c_i^*|^* \leq C i^{-1/p}$ and $p < 2$,

$$1007 \quad \sum_{i>N} (|c_i^*|^*)^2 \leq C^2 \sum_{i>N} i^{-2/p} = \mathcal{O}(N^{1 - \frac{2}{p}}),$$

1009 hence the norm error (square root) is $\mathcal{O}(N^{\frac{1}{2} - \frac{1}{p}})$. \square

1012 D.4 LEARNING AND DISCRETIZATION ERRORS

1013 **Assumption D.8.** Each \hat{c}_i is obtained by ERM over m i.i.d. frequency samples using a hypothesis
 1014 class with effective capacity d_{eff} under sub-Gaussian noise, so that
 1015

$$1016 \quad \mathbb{E}[\hat{c}_i - c_i^*] = \mathcal{O}\left(\sqrt{\frac{d_{\text{eff}}}{m}}\right). \quad (34)$$

1018 **Lemma D.9.** Let $\langle \cdot, \cdot \rangle_{\tilde{N}}$ be a discrete inner product (e.g., uniform frequency grid) that is a consistent
 1019 quadrature for $\langle \cdot, \cdot \rangle_{\mathcal{H}}$ on the class generated by $\{s\} \cup \{\mathcal{B}_i\}$. Then there exists $\varepsilon_{\text{disc}}(\tilde{N}) \downarrow 0$ such
 1020 that

$$1021 \quad |\langle f, g \rangle_{\mathcal{H}} - \langle f, g \rangle_{\tilde{N}}| \leq \varepsilon_{\text{disc}}(\tilde{N}) \quad \text{for all } f \in \{s\}, g \in \{\mathcal{B}_i\}_{i \geq 1}. \quad (35)$$

1023 *Proof.* Since point evaluations are continuous linear functionals in an RKHS and the involved functions
 1024 are continuous on compact subsets, standard quadrature consistency yields 35. (If f, g are
 1025 analytic in an annulus around the unit circle, one gets exponential rates; under Sobolev regularity,
 algebraic rates.) \square

1026
1027 **Theorem D.10.** *Under Assumptions D.1 and D.8 and Lemma D.9, the AFMO output after N blocks
1028 and \tilde{N} grid points satisfies*

1029
1030
$$\|u^* - \hat{u}_{N,\theta}\| \leq L_{\mathcal{Q}} \left(E_N(s) + \Delta_{pole}(N) + \left(\sum_{i=1}^N |\hat{c}_i - c_i^*|^2 \right)^{1/2} \right) + \varepsilon_{disc}(\tilde{N}), \quad (36)$$

1031

1032 with $\mathbb{E}[|\hat{c}_i - c_i^*|] = \mathcal{O}(\sqrt{d_{\text{eff}}/m})$ and $\varepsilon_{disc}(\tilde{N}) \rightarrow 0$ as $\tilde{N} \rightarrow \infty$.

1033
1034 *Proof.* Apply Theorem D.6 to bound the latent \mathcal{H} -error. Then use Lipschitz continuity of \mathcal{Q} to
1035 transfer the bound to the output space. The discretization error adds $\varepsilon_{disc}(\tilde{N})$ due to 35. \square
1036

1037 D.5 STABILITY TO POLE PERTURBATIONS

1038
1039 **Lemma D.11.** *For $a, b \in \mathbb{D}$ and $z \in \mathbb{D}$,*

1040
1041
$$\left| \frac{1}{1 - \bar{a}z} - \frac{1}{1 - \bar{b}z} \right| \leq \frac{|a - b|}{(1 - |a|)(1 - |b|)}, \quad (37)$$

1042

1043
1044
$$\left| \sqrt{1 - |a|^2} - \sqrt{1 - |b|^2} \right| \leq \frac{|a - b|}{\sqrt{1 - \max\{|a|, |b|\}^2}}, \quad (38)$$

1045

1046 and for $F(z; a) = \frac{z - a}{1 - \bar{a}z}$,

1047
1048
$$|F(z; a) - F(z; b)| \leq \frac{4|a - b|}{(1 - |a|)(1 - |b|)}, \quad |F(z; a)| \leq 1. \quad (39)$$

1049

1050 *Proof.* For 37,

1051
1052
$$\frac{1}{1 - \bar{a}z} - \frac{1}{1 - \bar{b}z} = \frac{(\bar{a} - \bar{b})z}{(1 - \bar{a}z)(1 - \bar{b}z)},$$

1053

1054 and $|1 - \bar{a}z| \geq 1 - |a||z| \geq 1 - |a|, |z| \leq 1$, yielding the bound. For 38, use the mean-value theorem
1055 on $x \mapsto \sqrt{1 - x}$ with $x = |a|^2, |b|^2$ and $||a|^2 - |b|^2| \leq |a - b|(|a| + |b|) \leq 2|a - b|$. For 39, expand
1056

1057
1058
$$F(z; a) - F(z; b) = \frac{(b - a) + (\bar{a} - \bar{b})z^2 + (a\bar{b} - b\bar{a})z}{(1 - \bar{a}z)(1 - \bar{b}z)},$$

1059

1060 and bound the numerator by $C|a - b|$ for $|z| \leq 1$, while the denominator is bounded below by
1061 $(1 - |a|)(1 - |b|)$. \square

1062 **Theorem D.12.** *Let $a_{1:i}, \tilde{a}_{1:i} \in \mathbb{D}$ with $|\tilde{a}_j - a_j| \leq \delta_j$. Then there exist constants $C_i > 0$ (depending
1063 on $a_{1:i}$) such that*

1064
1065
$$\|\mathcal{B}_i(\cdot; \tilde{a}_{1:i}) - \mathcal{B}_i(\cdot; a_{1:i})\|_{\mathcal{H}} \leq C_i \sum_{j=1}^i \frac{\delta_j}{1 - |a_j|}. \quad (40)$$

1066

1067 Consequently, for any coefficients \hat{c}_i ,

1068
1069
$$\left\| \sum_{i=1}^N \hat{c}_i \mathcal{B}_i(\cdot; \tilde{a}_{1:i}) - \sum_{i=1}^N \hat{c}_i \mathcal{B}_i(\cdot; a_{1:i}) \right\|_{\mathcal{H}} \leq \left(\sum_{i=1}^N |\hat{c}_i| C_i \right) \left(\sum_{j=1}^N \frac{\delta_j}{1 - |a_j|} \right). \quad (41)$$

1070

1071 *Proof.* Write

1072
1073
$$\mathcal{B}_i(\cdot; a_{1:i}) = e_{a_i} \prod_{j=1}^{i-1} F(\cdot; a_j), \quad \mathcal{B}_i(\cdot; \tilde{a}_{1:i}) = e_{\tilde{a}_i} \prod_{j=1}^{i-1} F(\cdot; \tilde{a}_j).$$

1074

1075 Use the product telescoping identity

1076
1077
$$\prod_{k=1}^i P_k - \prod_{k=1}^i Q_k = \sum_{k=1}^i \left(\prod_{j < k} P_j \right) (P_k - Q_k) \left(\prod_{j > k} Q_j \right),$$

1080 with $P_1 = e_{\tilde{a}_i}$, $Q_1 = e_{a_i}$, and $P_k = F(\cdot; \tilde{a}_{k-1})$, $Q_k = F(\cdot; a_{k-1})$ for $k \geq 2$. Taking sup-norms on
 1081 \mathbb{D} and using $|F(\cdot; a)| \leq 1$,
 1082

$$1083 \quad \|\mathcal{B}_i(\cdot; \tilde{a}_{1:i}) - \mathcal{B}_i(\cdot; a_{1:i})\|_\infty \leq \|e_{\tilde{a}_i} - e_{a_i}\|_\infty + \sum_{j=1}^{i-1} \|F(\cdot; \tilde{a}_j) - F(\cdot; a_j)\|_\infty.$$

1086 Apply Lemma D.11 to bound each term by a constant times $\delta_j/(1 - |a_j|)$. Since evaluation func-
 1087 tionals are continuous and the kernel is bounded on compact subsets, there exists an embedding
 1088 constant C_{emb} with $\|f\|_{\mathcal{H}} \leq C_{\text{emb}}\|f\|_\infty$ on the set considered; thus 40 follows with C_i absorbing
 1089 all constants. Finally,

$$1090 \quad \left\| \sum_{i=1}^N \tilde{c}_i (\mathcal{B}_i(\cdot; \tilde{a}_{1:i}) - \mathcal{B}_i(\cdot; a_{1:i})) \right\|_{\mathcal{H}} \leq \sum_{i=1}^N |\tilde{c}_i| \|\mathcal{B}_i(\cdot; \tilde{a}_{1:i}) - \mathcal{B}_i(\cdot; a_{1:i})\|_{\mathcal{H}},$$

1093 giving 41. \square

1095 D.6 END-TO-END CONVERGENCE WITHOUT GREEDY SELECTION

1097 **Theorem D.13.** *Assume:*

- 1099 1. $s \in K_B$;
- 1100 2. $\sum_{i=1}^{\infty} \mathbb{E}[\|\tilde{c}_i - c_i^*\|^2]^{1/2} < \infty$ (as sample size $m \rightarrow \infty$ and model capacity increase);
- 1102 3. $\varepsilon_{\text{disc}}(\tilde{N}) \rightarrow 0$ as $\tilde{N} \rightarrow \infty$.

1103 Then

$$1104 \quad \lim_{N \rightarrow \infty} \|u^* - \hat{u}_{N,\theta}\| = 0.$$

1107 *Proof.* Since $s \in K_B$ and $\{\mathcal{B}_i\}$ is an ONB of K_B , Theorem D.4 gives $s_N \rightarrow s$ in \mathcal{H} . In 36, for this
 1108 fixed pole sequence one has $E_N(s) = \Delta_{\text{pole}}(N) = 0$. Using (2) and (3), we obtain $\|u^* - \hat{u}_{N,\theta}\| \rightarrow$
 1109 0. \square

1110 D.7 CONNECTION OF SSM TO CORRELATION AND AFMO OUTPUT

1112 **Proposition D.14.** *With $H_i(e^{i\omega}) = \overline{\mathcal{B}_i(e^{i\omega})}$, the i -th SSM block computes $\tilde{c}_i \approx \langle z_i, \mathcal{B}_i \rangle_{\mathcal{H}}$. Hence,
 1113 by Lemma D.2, after N blocks*

$$1115 \quad z_{N+1} = \sum_{i=1}^N \tilde{c}_i \mathcal{B}_i, \quad \hat{u}_{N,\theta} = \mathcal{Q}(z_{N+1}). \quad (42)$$

1118 *Proof.* The coefficient claim follows from Lemma D.3 applied to z_i in place of s . The aggregation
 1119 identity is Lemma D.2. The last equality is the definition of \mathcal{Q} . \square

1121 **Corollary D.15.** *All latent-space error bounds transfer to the PDE output space via*

$$1123 \quad \|u^* - \hat{u}_{N,\theta}\| \leq L_{\mathcal{Q}} \left\| s - \sum_{i=1}^N \tilde{c}_i \mathcal{B}_i \right\| + \varepsilon_{\text{disc}}(\tilde{N}).$$

1126 E TRANSFER FUNCTION

1128 We consider a (finite) Blaschke product

$$1130 \quad H(z) = \prod_{j=1}^n \frac{1 - p_j z}{z - p_j}, \quad |p_j| < 1, \quad (43)$$

1133 and convert it into a single ratio of polynomials whose coefficients match the parameterization used
 to train SSMs.

1134 **Polynomial expansion and z^{-1} form.** Denote numerator and denominator polynomials
 1135

$$1136 \quad B_{\text{poly}}(z) = \prod_{j=1}^n (z - p_j), \quad A_{\text{poly}}(z) = \prod_{j=1}^n (1 - p_j z), \quad (44)$$

$$1137$$

$$1138$$

1139 so that $H(z) = \frac{A_{\text{poly}}(z)}{B_{\text{poly}}(z)}$. Let $d = \deg B_{\text{poly}} = \deg A_{\text{poly}} = n$. To obtain the form with a unit
 1140 constant term in the denominator, divide numerator and denominator by z^d and then normalize:
 1141

$$1142 \quad \tilde{H}(z) = \frac{\sum_{k=0}^d \alpha_k z^{-k}}{\sum_{k=0}^d \beta_k z^{-k}} \xrightarrow{\text{normalize}} h_0 + \sum_{k=1}^d \frac{b_k}{1} z^{-k} \Big/ \left(1 + \sum_{k=1}^d a_k z^{-k}\right). \quad (45)$$

$$1143$$

$$1144$$

1145 The SSM coefficients are then reduced as:
 1146

$$1147 \quad h_0 = \frac{\alpha_0}{\beta_0}, \quad b_k = \frac{\alpha_k}{\beta_0}, \quad a_k = \frac{\beta_k}{\beta_0}, \quad k = 1, \dots, d.$$

$$1148$$

1149 **Example ($n = 2$).** With $p_1, p_2 \in \mathbb{C}$, expand
 1150

$$1151 \quad B_{\text{poly}}(z) = (z - p_1)(z - p_2) = z^2 - (p_1 + p_2)z + p_1 p_2,$$

$$1152$$

$$1153 \quad A_{\text{poly}}(z) = (1 - p_1 z)(1 - p_2 z) = 1 - (p_1 + p_2)z + (p_1 p_2)z^2.$$

$$1154$$

1155 Divide by z^2 to get polynomials in z^{-1} and normalize by the denominator's constant term ($\beta_0 = p_1 p_2$), yielding
 1156

$$1157 \quad H(z) = \frac{1 - (p_1 + p_2)z^{-1} + (p_1 p_2)z^{-2}}{p_1 p_2 - (p_1 + p_2)z^{-1} + z^{-2}} = \frac{h_0 + b_1 z^{-1} + b_2 z^{-2}}{1 + a_1 z^{-1} + a_2 z^{-2}},$$

$$1158$$

1159 with

$$1160 \quad h_0 = \frac{1}{p_1 p_2}, \quad b_1 = -\frac{p_1 + p_2}{p_1 p_2}, \quad b_2 = 1, \quad a_1 = -\frac{p_1 + p_2}{p_1 p_2}, \quad a_2 = \frac{1}{p_1 p_2}.$$

$$1161$$

1162 **Efficient computation for large n .** Direct symbolic expansion scales poorly. Instead, we multiply
 1163 degree-1 polynomials using FFT-based convolution. Represent each factor by its coefficient vector:
 1164

$$1165 \quad (z - p_j) \leftrightarrow [1, -p_j], \quad (1 - p_j z) \leftrightarrow [1, -p_j],$$

$$1166$$

1167 and iteratively convolve to form B_{poly} and A_{poly} . By the convolution theorem, polynomial multipli-
 1168 cation is element-wise in the frequency domain, giving $\mathcal{O}(d \log d)$ complexity. After both polyno-
 1169 mials are assembled, convert to z^{-1} by dividing by z^d , then normalize by the denominator's constant
 1170 term to obtain $(h_0, \{a_k\}, \{b_k\})$ as in 45.

$$1171$$

$$1172$$

$$1173$$

$$1174$$

$$1175$$

$$1176$$

$$1177$$

$$1178$$

$$1179$$

$$1180$$

$$1181$$

$$1182$$

$$1183$$

$$1184$$

$$1185$$

$$1186$$

$$1187$$